

# Lung Tissue Biomechanics Imaged with Synchrotron Phase Contrast Microtomography in Live Rats

**Jose-Luis Cercos-Pita**

Uppsala University

**Luca Fardin**

European Synchrotron Radiation Facility

**Hugo Leclerc**

Université Paris-Saclay

**Bertrand Maury**

Université PSL

**Gaetano Perchiazzi**

Uppsala University

**Alberto Bravin**

European Synchrotron Radiation Facility

**Sam Bayat** (✉ [sbayat@chu-grenoble.fr](mailto:sbayat@chu-grenoble.fr))

Univ. Grenoble Alpes, Synchrotron Radiation for Biomedicine STROBE Inserm UA07

---

## Research Article

**Keywords:** Respiration, Artificial; Respiratory Distress Syndrome, Adult; Tomography, X-Ray Computed; Synchrotrons; Pulmonary alveoli.

**Posted Date:** October 27th, 2021

**DOI:** <https://doi.org/10.21203/rs.3.rs-970496/v1>

**License:** © ⓘ This work is licensed under a Creative Commons Attribution 4.0 International License.

[Read Full License](#)

---

**Version of Record:** A version of this preprint was published at Scientific Reports on March 23rd, 2022. See the published version at <https://doi.org/10.1038/s41598-022-09052-9>.

# Abstract

The magnitude and distribution of strain imposed on the peripheral airspaces by mechanical ventilation at the microscopic level and the consequent deformations are unknown despite their importance for understanding the mechanisms occurring at the onset of ventilator-induced lung injury. Here a 4-Dimensional (3D + time) image acquisition and processing technique is developed to assess pulmonary acinar biomechanics at microscopic resolution. Synchrotron radiation phase contrast CT with an isotropic voxel size of  $6 \mu\text{m}^3$  is applied in live anesthetized rats under controlled mechanical ventilation. Video animations of regional acinar and vascular strain are acquired *in vivo*. Maps of strain distribution due to positive-pressure breaths in lung acini and blood vessels are derived based on CT images. Regional strain within the lung peripheral airspaces takes average values of  $0.09 \pm 0.02$ . Fitting the expression  $S=kV^n$ , to the changes in peripheral airspace area ( $S$ ) and volume ( $V$ ) during a positive pressure breath yields an exponent  $n = 0.82 \pm 0.03$ , suggesting predominant alveolar expansion rather than ductal expansion or alveolar recruitment. We conclude that this methodology can be used to assess acinar conformational changes during positive pressure breaths in intact peripheral lung airspaces

## Introduction

Mechanical ventilation used during anaesthesia or in acute respiratory failure causes or worsens strain-induced lung tissue injury <sup>1</sup>. It is generally agreed that excessive mechanical strain due to inflation <sup>2</sup>, cyclic recruitment-derecruitment <sup>3</sup>, increased energy dissipation within the parenchyma <sup>4</sup> and associated inflammation <sup>5</sup> are contributing factors. The magnitude and distribution of strain imposed on the peripheral airspaces by mechanical ventilation at the microscopic level and the resulting deformation of peripheral airspaces are unknown despite their importance for understanding the mechanism occurring at the onset of ventilator-induced lung injury (VILI). Indeed, a fundamental question that has remained elusive for decades is how the lung acinus expands with lung inflation <sup>6</sup>. This question is particularly pressing in the context of severe acute respiratory syndrome due to coronavirus-2 pandemic (SARS-CoV-2) where VILI has been recognized as a contributing factor to patient morbidity and mortality <sup>7</sup>.

Imaging methods for high resolution *in vivo* assessment of peripheral airspace deformation and its regional dynamics are lacking. The reason lies in the difficulty of determining effective structural deformation, due to the motion blurring at microscopic resolution, which is induced by respiration and cardiovascular activity. Different imaging modalities such as optical coherence tomography (OCT) <sup>8,9</sup>, ultrasound (US) <sup>10</sup>, magnetic resonance tomography <sup>11</sup> (MRI) and X-ray computed tomography (CT) <sup>12</sup> have been used to quantify regional tissue strain, or the normalized deformation of a tissue that changes shape or volume following mechanical loading over time. Because of the limitations in tissue penetration (US, OCT) and spatial resolution (US, MRI), X-ray imaging is the most suitable modality for imaging the lung tissue morphology. However, in its practical implementation, a compromise is made between the spatial resolution, temporal resolution, size of the imaging field and sensitivity.

Here we extend 4D-CT of lung tissue biomechanics to microscopic length scales in live anesthetized rats under controlled mechanical ventilation. To minimize motion blurring occurring *in vivo*, four-dimensional x-ray CT (4D-CT) imaging has been developed<sup>13-16</sup>. This approach refers to sequential acquisition of 3D images with prospective gating or retrospective sorting of image projections with respect to a periodic motion. We use phase-contrast imaging with radiation produced with a synchrotron source, and a combination of technological advances including a fast-imaging camera connected to optics allowing an isotropic voxel size of  $6\ \mu\text{m}^3$ <sup>17</sup>. We applied this methodology to acquire maps of strain distribution due to positive-pressure breaths in the lung acini and in blood vessels. We show that this methodology can be used to assess conformational changes during positive pressure breaths in intact peripheral lung airspaces *in vivo*.

## Results

### Dynamic synchrotron phase contrast *in vivo* microtomography

Available methods based on X-ray attenuation using commercial X-ray sources have significant limitations arising from low available X-ray flux, which sets limits to the achievable spatial resolution, and prolongs acquisition time. Moreover, the lung being an air-filled organ weakly attenuates X-rays which reduces sensitivity. In this study, we used phase-contrast imaging with radiation produced with a synchrotron source. Due to its high intensity, which is orders of magnitude higher than conventional sources, synchrotron radiation allows improving the temporal and spatial resolution of 4D-CT imaging, performing 4D  $1\text{-}10\ \mu\text{m}^3$  voxel size CT imaging in the temporal scale of minutes. Due to the strong cardiac-induced deformations, the alveolar structures often do not return to the same position at end-expiration, which makes micro tomography very challenging at micrometric spatial resolutions, using 4DCT<sup>15</sup>. Here we used a combination of a fast-imaging camera connected to optics allowing an isotropic voxel size of  $6\ \mu\text{m}^3$  (Figure 1), combined with triggering of breathing by the electrocardiographic and respiratory signals. Moreover, we implemented an open software environment for 3D mapping of lung acinar and vascular biomechanics. We acquired 4D volumetric phase-contrast microtomographic images in 3 healthy anesthetized and mechanically ventilated rats *in vivo*. Sequential 3D CT images covering a field of view of  $15.36 \cdot 15.36 \cdot 1.2\ \text{mm}^3$  were reconstructed at 10 ms time intervals over one entire breath lasting  $760 \pm 10$  ms. We show a video of the structural deformation of the lung within the respiratory cycle (**Supporting video 1**).

### Mapping dynamic strain within lung airspaces and blood vessels

*Dynamic strain maps of airspaces and blood vessels are shown in Supporting video 2 and 3, respectively. Mean recorded mechanical ventilation parameters were: maximal airway pressure ( $P_{\text{max}}$ ):  $11.6 \pm 1.1$*

*cmH<sub>2</sub>O; positive end-expiratory pressure (PEEP): 5.9 ± 0.3 cmH<sub>2</sub>O; driving pressure (P<sub>max</sub> – PEEP): 5.7 ± 0.8 cmH<sub>2</sub>O; respiratory rate: 72 ± 7.2 bpm; tidal volume: 2.8 ± 0.2 ml/kg. Figure 2 shows still 2D axial slices of the lung morphology, as well as maps of local strain within the airspaces and vascular structures at 3 successive time points within the respiratory cycle. The selected ROI's in one animal are shown in Figure 3A. Figure 3B demonstrates the quality of a sample acinar segmentation. Figures 3C and D show the evolution of strain within the selected ROI's in airspaces and blood vessels, respectively. We found an average maximal regional lung strain within the airspaces of 0.09 ± 0.02.*

## **Ventilation-induced changes in lung airspace conformation**

The evolution of the volume (V) and internal surface area (S) of the segmented acini within a representative ROI throughout a respiratory cycle is shown in Figure 4, as well as a log-log plot of S against V. Table 1 shows the values of the exponent  $n$  calculated by fitting the expression  $S = kV^n$ , to the changes in acinar surface area and volume during a positive pressure breath from an average PEEP of 6 to an average peak airway pressure of 12 cmH<sub>2</sub>O and back. The mean value of this exponent was 0.82 ± 0.03.

Table 1  
 Values of exponent  $n$  calculated  
 by fitting the expression  
 $S = kV^n$ , to the changes in  
 acinar surface area (S) and  
 volume (V) during a positive  
 pressure inspiration from 6 to 12  
 cmH<sub>2</sub>O.

<i>Rat</i>	<i>ROI<sup>a</sup></i>	<i>n</i>
R7	1	0.85
R7	2	0.82
R7	3	0.85
R7	4	0.81
R7	5	0.80
R8	1	0.80
R8	2	0.76
R8	3	0.84
R9	1	0.87
R9	2	0.84
R9	3	0.81
R9	4	0.84
m ± SD		0.82 ± 0.03
a) Region of Interest.		

So far, the changes in lung acinar shape as a function of lung inflation have been assessed post-mortem in fixed or frozen tissue samples using light microscopy and electron microscopy<sup>18-20</sup>. Post-mortem light microscopic measurements of fixed or frozen lungs have found conflicting results regarding the configurational changes of lung acini with lung inflation. Some have suggested that alveoli expand isotropically<sup>21</sup>. This means that linear dimensions of alveolar structures vary as the cube root of lung volume ( $V^{1/3}$ ). Others however, have found some degree of anisotropic expansion with the alveolar duct volume changing proportionately more than alveolar volume<sup>22</sup>. Previously, Carney et al. investigated the mechanical behavior of subpleural alveoli during lung inflation *in vivo*, using intravital microscopy through a thoracotomy incision in dogs<sup>8</sup>. They found that above 20% TLC, alveolar volume remained stable while an increasing number of alveoli were recruited and concluded that lung volume changes predominantly occurred as a result of alveolar recruitment. However, in their study alveolar mechanics was analyzed in initially degassed lungs in open chest animals which may have promoted alveolar

collapse. Using intravital microscopy and optical coherence microscopy (OCT), Mertens et al. investigated alveolar dynamics through a pleural window in open-chest mice with normal and injured lungs<sup>23</sup>. They found that alveolar distension rather than recruitment was the main mechanism of lung inflation. Besides species and methodological differences that may explain the discrepancy in the data from intravital microscopy in these and other studies<sup>24-26</sup>, there has been concern that the mechanical behavior of subpleural alveoli may be different from those deep in the lung.

One approach to describe how the conformation of terminal airspaces is altered by inflation, is to determine the changes in the surface area of airspaces in proportion to volume. With a perfectly isotropic expansion, surface area necessarily increases in proportion to  $V^{2/3}$  ( $n=0.67$ ) because surface area varies as the square and volume as the cube of a characteristic linear dimension. Departure from this value would indicate a configurational change of the acinus with inflation<sup>27</sup>. Assuming an acinar structure with an axial duct from which alveoli open radially, the relative shape and changes in ductal and alveolar volumes result in different overall surface changes relative to volume. Based on this approach in lungs fixed at different volumes, Gil et al.<sup>28</sup> described different mechanisms of acinar configurational changes: 1) sequential recruitment-derecruitment ( $n=1$ ); 2) isotropic balloonlike inflation ( $n=0.67$ ); 3) simultaneous change in alveolar size and shape, e.g.: from dodecahedral to spherical, due to alveolar septal unpleating ( $n>0.67$ ); 4) crumpling of the alveolar surface with anisotropic, accordion-like deformations of the entire peripheral airspace units ( $n=1$ ). The results of Gil et al. suggested that although all these mechanisms are involved, they tended to occur at different lung volumes. At lower lung volumes, deformation occurred predominantly within the alveolar ducts ( $S=kV^{0.33}$ ), while at higher lung volumes, alveolar inflation predominated, with simultaneous change in alveolar shape and volume. Because of the limitations of current imaging techniques, to date this issue has not been investigated in deep lung acini *in vivo*<sup>6</sup>. Sera et al. investigated lung acinar dynamics in post-mortem mice without tissue fixation in static conditions, using synchrotron phase-contrast microtomography<sup>29</sup>. They found that the alveolar duct diameter changed dramatically during inflation at low pressures and remained relatively constant above an airway pressure of  $\sim 8$  cmH<sub>2</sub>O, where alveolar inflation predominated with  $S=kV^{0.87}$ <sup>29</sup>. The findings of the present study ( $S=kV^{0.82}$ ) while obtained *in vivo* and in dynamic conditions under realistic mechanical ventilation settings are very similar to those of Sera et al. at airway pressures  $> 8$  cmH<sub>2</sub>O. This finding is indicative of an anisotropic behavior of the overall lung acinus, where the stress-strain relation in alveolar ducts, mainly determined by high densities of connective tissue situated around the alveolar mouths<sup>30-32</sup>, is different from that of alveoli, determined by the connective tissue within the alveolar septa as well the surface tension properties of the air-liquid interface<sup>33</sup>. A schematic illustration of the how acinar conformation changes result in different exponents in  $S=kV^n$  is provided in Figure 5.

## Conclusions

We developed a 4D synchrotron phase-contrast micro-CT technique allowing for the *in vivo* assessment of the expansion of lung acini with an isotropic  $6 \mu\text{m}^3$  voxel size, which to our knowledge is the highest

achieved so far. We found that under the applied mechanical ventilation settings, regional lung strain within the lung peripheral airspaces took values of  $0.09 \pm 0.02$  in anesthetized rats. Our data suggest that the conformational changes in lung airspaces are indicative of predominant alveolar expansion rather than ductal expansion or alveolar recruitment. We further analyzed the deformation in pulmonary blood vessels and found a large disparity depending on caliber. We believe this methodology will be instrumental in advancing our understanding of the dynamics of stress and strain within the lung parenchyma under mechanical ventilation and devising ventilation modes to preserve the lung parenchyma from stretch-induced injury.

## Methods

*Synchrotron radiation imaging:* The experiments were performed at the biomedical beamline (ID-17) of the European Synchrotron Radiation Facility (ESRF, Grenoble, France). Briefly, X-rays produced by a multipole wiggler were monochromatized using a double bent Laue Si (111) monochromator<sup>34</sup>, selecting a photon energy of 40 keV. Monochromatic radiation impinged on the sample 146 m from the source and was detected by a fast Complementary metal–oxide–semiconductor (CMOS) PCO Edge 5.5 camera (PCO AG, Kelheim, Germany) coupled to a 250  $\mu\text{m}$  thick Cerium-doped Lutetium Aluminum Garnet (LuAG:Ce) scintillator and optics yielding an isotropic pixel size of 6  $\mu\text{m}^2$ . The field of view of the camera was reduced to 15.4 · 1.2  $\text{mm}^2$  to achieve a frame rate of 500 fps, as a compromise between field of view and temporal resolution. The sample to detector distance was set to 4m to utilize propagation-based phase contrast imaging<sup>35</sup>.

*Animal preparation:* The care of animals and the experimental procedures were in accordance with the Directive 2010/63/EU of the European Parliament on the protection of animals used for scientific purposes, complied with the ARRIVE guidelines<sup>36</sup> and were approved by the ESRF Ethical Committee on Animal Experimentation (Comité d'éthique en expérimentation animale; ETHAX #113) and the French Ministry of Higher Education and Research under the number: 2017071816174477. The study was performed on 3 female OFA rats (*Ratus Norvegicus*, Wt:  $253.7 \pm 7.2$  g). Anesthesia was induced by intra-peritoneal injection of 1.5 to 2 ml  $\text{kg}^{-1}$  body weight of a solution containing Ketamine (40 mg  $\text{ml}^{-1}$ ) and Xylazine (20 mg  $\text{ml}^{-1}$ ). The animal was tracheostomized and a 14 G polyethylene catheter (Venflon; Becton Dickinson, Le Pont-de-Claix, France) was inserted and secured with a gas-tight seal. A 26 G polyethylene catheter (Neoflon; Becton Dickinson, Helsingborg, Sweden) was inserted in the jugular vein. After surgery, the animal was immobilized in the vertical position in a custom-made plastic holder and placed on a remote-controlled rotation stage in the experimental hutch for imaging. Anesthesia was maintained during the duration of the experiment with 1% inhaled isoflurane (Isoflurane Belamont, Piramal Critical Care). The animals were mechanically ventilated with a tidal volume of 8 ml  $\text{kg}^{-1}$ ,  $\text{FiO}_2 = 0.5$ ; PEEP = 6  $\text{cmH}_2\text{O}$ . After verifying adequate depth of anesthesia (heart rate stability, inhibition of response to limb stimulation), muscle relaxation was induced by Atracurium injection (4 mg  $\text{kg}^{-1}$ ) to avoid motion and suppress spontaneous breathing. The electrocardiogram (ECG), airway pressure and air

flow were continuously sampled at 10 kHz and recorded using a Powerlab 16/35 data acquisition device (DAQ, Adinstruments, Dunedin, New Zealand) (Figure S1).

## Image acquisition protocol

The image acquisition protocol was described in detail in a previous publication<sup>5</sup>. It was based on the synchronization between the heartbeat and the mechanical ventilation, which ensured a periodic lung parenchymal motion, as required by dynamic CT acquisitions. Briefly, the ECG signal was processed in real-time with a peak detector, which generated a square signal of predefined length and duty cycle when a R wave was detected, at the time instant  $t_i$ . The square signal was transmitted to the mechanical ventilator controller, to trigger an assisted breath. The R wave detection was disabled for the whole duration of the square signal. In the specific experiment discussed here, the square signal duration was  $s$  and the heartbeat period was  $s$ , implying heartbeats per respiratory cycle. A full tomographic scan consisted of a set of 250000 projections acquired over 180 degrees during a single sample half-rotation. A constant angular velocity,  $^\circ \text{ s}^{-1}$  was set to include approximately 700 respiratory cycles per scan.

Image reconstruction: The image processing workflow is shown in Supplemental Figure S2. A retrospective gating methodology<sup>37</sup> was used to reconstruct 4-Dimensional (3D + time) CT images. In this approach each projection:  $P(\alpha, t^*)$ , is characterized by an angle,  $\alpha = \omega(t - t_0)$ , and a time:  $t^* = t - t_{j \text{ n}_{ECG}}$ , where  $t_{j \text{ n}_{ECG}}$  is the time at which j-th respiratory cycle was started:

$$t_{j \text{ n}_{ECG}} < t < t_{(j+1) \text{ n}_{ECG}} \quad (1)$$

The projections corresponding to the same time interval were sorted in 3D image stacks discretizing  $t^*$  with a  $\Delta t = 10\text{ms}$  time resolution. Tomographic reconstruction was performed with a Filtered Back Projection algorithm using PyHST2<sup>38</sup> software, after application of Paganin's single material phase retrieval algorithm<sup>39</sup>. Since the ECG signal is not perfectly periodic, the projections were not equally spaced. Hence, 78 3D-CTs were finally reconstructed.

## Image segmentation

The same segmentation process was used for blood vessels air airspaces. The Otsu's algorithm allows for a first partitioning of air and non-air voxels<sup>40</sup>, starting from the image histogram. To classify the former voxels as proximal, intermediate and terminal, an iterative process was carried out. At each step of a 3D erosion process, the number of removed voxels was stored in a list. Assuming the primary bronchi are not far from cylinders, it is expected that a large subset of the values in this list is piecewise linear with respect to the index. Thus, the identification of the linear parts in this list using linear regression and RMSE, allows to classify the central parts of the bronchi, starting from the largest, to the smallest ones. Voxels are then dilated to end the classification of these proximal parts. Intermediate structures are subsequently identified by means of dilation, erosion and hole filling using voxels from the primary

structures. All the selected voxels which were not classified as proximal or intermediate were classified as terminal structures, with a similar approach as the ones described previously in the literature<sup>41,42</sup>. Using this method, terminal airways as well as the proximal and intermediate blood vessels were identified. Occasionally, additional manual editing was performed as necessary by adding markers on the image and carrying out a watershed.

## Image registration

A non-rigid registration algorithm was used in order to deform the segmented airspace or vascular volumes in a pairwise fashion, between each time step and the immediately previous one. The registration algorithm applies a B-spline grid to represent the original segmented greyscale volume. It was initially proposed by Klein et al.<sup>43</sup> and is published within the Python Image Registration Toolkit (PIRT)<sup>44</sup>. A Sum of Squared Differences (SSD) similarity metric was applied, as well as a Laplacian regularization term. The registration algorithm was applied in a pairwise fashion, between each time step and the immediately previous one. This displacement field, was then converted to a Lagrangian displacement field representing the deformation between each image with the first one, through the following recursive process

$$\mathbf{r}(n\Delta t) = \mathbf{x} + \mathbf{u}(\mathbf{x}; 0, n\Delta t) \quad (2)$$

$$\mathbf{u}(\mathbf{x}; 0, n\Delta t) = \mathbf{u}(\mathbf{x}; 0, (n-1)\Delta t) + \mathbf{u}^*(\mathbf{r}(n\Delta t); (n-1)\Delta t, n\Delta t) \quad (3)$$

This two-step computation of the displacement field allowed to minimize registration errors. An error value was defined, as:

$$\varepsilon_u(\mathbf{x}) = \frac{\mathbf{u}(\mathbf{x}; 0, T) - \mathbf{u}^*(\mathbf{x}; 0, T)}{\max(\mathbf{u}^*(\mathbf{x}; 0, T))} \quad (4)$$

Which was used to assess the quality of the registration.

We investigated whether completely deflated airspaces were inflated upon inspiration, a phenomenon referred to as “recruitment”. To this end, we used skeletonization, a process that reduces binary objects to 1-pixel wide representations, in order to extract the airspace topology. This was performed with the Skeletonize\_3D toolkit (<https://scikit-image.org>)<sup>45</sup>. Skeletons were produced for the segmented airspace volume at each time instant,  $\mathbf{s}(\mathbf{x}; \Omega(n\Delta t))$ . The skeleton of the first time instant was deformed according the Lagrangian displacement field,  $\mathbf{s}(\mathbf{x}; \Omega(n\Delta t))$ <sup>46</sup> Each pair of skeletons,  $\mathbf{s}(\mathbf{x}; \Omega(n\Delta t))$  and  $\mathbf{s}(\mathbf{r}(n\Delta t); \Omega(0))$  were compared by computing 2 distances, which were the distance between the skeleton and the segmented volume boundary:

$$d_{\Omega} = \min \{s(\mathbf{x}; \Omega(n\Delta t)), \partial\Omega(n\Delta t)\}c \quad (5)$$

and the distance between the two skeletons:

$$d_s = \min \{s(\mathbf{x}; \Omega(n\Delta t)), s(\mathbf{r}(n\Delta t); \Omega(0))\} \quad (6)$$

Recruited structures could then be eventually segmented by selecting initial seeds or voxels where  $d_s > d_{\Omega}$ . However, in this experiment, no recruited airspaces were detected.

### Computation of volume and surface change

The divergence theorem was applied to compute the volume change

$$\Delta v(n\Delta t) = \sum_{i \in \Omega} \langle \nabla \cdot \mathbf{u}(\mathbf{x}_i; 0, n\Delta t) \rangle \quad (7)$$

with  $\Omega$  the segmented voxels at the first time point in the respiratory cycle. To overcome the limitations of traditional Jacobian computations<sup>47</sup>, a high order Mean Least Squares (MLS) kernel-based convolution was applied<sup>48</sup>, which grants linear consistency:

$$\langle \nabla \cdot \mathbf{u}(\mathbf{x}_i; 0, n\Delta t) \rangle = \sum_{j \in \Omega} \mathbf{u}(\mathbf{x}_j; 0, n\Delta t) \cdot (L(\mathbf{x}_i) \cdot \nabla W(\mathbf{x}_j - \mathbf{x}_i)) \quad (8)$$

Where  $W$  is the kernel convolution, and  $L$  is the MLS matrix which corrects the kernel compact support truncation:

$$L(\mathbf{x}_i) = \left[ \sum_{j \in \Omega} (\mathbf{x}_j - \mathbf{x}_i) \otimes \nabla W(\mathbf{x}_j - \mathbf{x}_i) \right]^{-1} \quad (9)$$

It should be noted that the convolution above considers only the segmented voxels. For the surface change computation, a similar expression was used, also based on the divergence theorem:

$$\Delta s(n\Delta t) = \sum_{i \in \Omega} \langle \nabla \cdot (\langle h(\mathbf{x}_i) \rangle \mathbf{u}(\mathbf{x}_i; 0, n\Delta t)) \rangle \quad (10)$$

With  $h$  the mean Gaussian curvature, redefined as a volumetric field<sup>49</sup>.

From the magnitudes involved in the expressions above, the only one depending on time is the displacement vector field,  $\mathbf{u}$ , obtained from the registration. All other magnitudes were computed in the initial time instant.

# Declarations

**Acknowledgments:** The authors wish to thank Herwig Requardt and ESRF ID-17 staff for technical assistance.

**Author Contributions:** AB, BM, GP, LF and SB conceived the study; AB, JLCP, LF and SB acquired the data; AB, BM, JLCP, HL, LF, and SB analysed image data; AB, BM, JLCP, HL, LF, and SB interpreted the findings; SB and JLCP drafted the manuscript. All authors edited and approved the submitted manuscript.

**Competing Interest Statement:** The authors declare no competing financial interests related to this work.

**Data availability:** Data are available upon reasonable request to the corresponding author.

**Funding:** This work was supported by the Swedish Research Council (grant 2018-02438), the Swedish Heart-Lung Foundation (grant 20170531), the European Synchrotron Radiation Facility, by the French Institute of Health and Medical Research (INSERM UA07).

# References

1. Slutsky, A. S. & Ranieri, V. M. Ventilator-induced lung injury. *The New England journal of medicine* **369**, 2126-2136, doi:10.1056/NEJMra1208707 (2013).
2. Dreyfuss, D. & Saumon, G. Ventilator-induced lung injury: lessons from experimental studies. *Am J Respir Crit Care Med* **157**, 294-323 (1998).
3. Muscedere, J. G., Mullen, J. B., Gan, K. & Slutsky, A. S. Tidal ventilation at low airway pressures can augment lung injury. *Am J Respir Crit Care Med* **149**, 1327-1334, doi:10.1164/ajrccm.149.5.8173774 (1994).
4. Gattinoni, L. *et al.* Ventilator-related causes of lung injury: the mechanical power. *Intensive care medicine* **42**, 1567-1575 (2016).
5. Tremblay, L. N. & Slutsky, A. S. Ventilator-induced lung injury: from the bench to the bedside. *Intensive Care Med* **32**, 24-33, doi:10.1007/s00134-005-2817-8 (2006).
6. Smaldone, G. C. & Mitzner, W. Viewpoint: unresolved mysteries. *J Appl Physiol (1985)* **113**, 1945-1947, doi:10.1152/japplphysiol.00545.2012 (2012).
7. Gattinoni, L. *et al.* COVID-19 pneumonia: different respiratory treatments for different phenotypes? *Intensive Care Med* **46**, 1099-1102, doi:10.1007/s00134-020-06033-2 (2020).
8. Carney, D. E. *et al.* The Mechanism of Lung Volume Change during Mechanical Ventilation. *Am J Respir Crit Care Med* **160**, 1697-1702 (1999).
9. Mulligan, J. A., Untracht, G. R., Chandrasekaran, S. N., Brown, C. N. & Adie, S. G. Emerging approaches for high-resolution imaging of tissue biomechanics with optical coherence elastography. *IEEE Journal of Selected Topics in Quantum Electronics* **22**, 246-265 (2015).

10. Ozturk, A., Grajo, J. R., Dhyani, M., Anthony, B. W. & Samir, A. E. Principles of ultrasound elastography. *Abdom Radiol (NY)* **43**, 773-785, doi:10.1007/s00261-018-1475-6 (2018).
11. Petitclerc, L., Sebastiani, G., Gilbert, G., Cloutier, G. & Tang, A. Liver fibrosis: Review of current imaging and MRI quantification techniques. *Journal of Magnetic Resonance Imaging* **45**, 1276-1295 (2017).
12. Mohammadi, A. *et al.* Rapid CT-based Estimation of Articular Cartilage Biomechanics in the Knee Joint Without Cartilage Segmentation. *Annals of Biomedical Engineering*, 1-11 (2020).
13. Jacob, R., Carson, J. P. & Einstein, D. R. in *D30. NOVEL APPROACHES TO ASSESSING LUNG PATHOPHYSIOLOGY* A5589-A5589 (American Thoracic Society, 2012).
14. Mokso, R. *et al.* Four-dimensional in vivo X-ray microscopy with projection-guided gating. *Sci Rep* **5**, 8727, doi:10.1038/srep08727 (2015).
15. Sera, T. *et al.* Development of high-resolution 4D in vivo-CT for visualization of cardiac and respiratory deformations of small animals. *Physics in Medicine & Biology* **53**, 4285 (2008).
16. Preissner, M. *et al.* High resolution propagation-based imaging system for in vivo dynamic computed tomography of lungs in small animals. *Physics in Medicine & Biology* **63**, 08NT03 (2018).
17. Mittone, A. *et al.* Multiscale pink-beam microCT imaging at the ESRF-ID17 biomedical beamline. *J Synchrotron Radiat* **27**, 1347-1357, doi:10.1107/S160057752000911X (2020).
18. Bachofen, H., Schurch, S., Urbinelli, M. & Weibel, E. R. Relations among alveolar surface tension, surface area, volume, and recoil pressure. *J Appl Physiol (1985)* **62**, 1878-1887, doi:10.1152/jappl.1987.62.5.1878 (1987).
19. Weibel, E. R. Biomorphometry in physiological and pathological research. *Acta Med Pol* **23**, 115-125 (1982).
20. Greaves, I. A., Hildebrandt, J. & Hoppin Jr, F. G. Micromechanics of the lung. *Comprehensive Physiology*, 217-231 (2011).
21. Storey, W. F. & Staub, N. C. Ventilation of terminal air units. *Journal of applied physiology* **17**, 391-397 (1962).
22. Klingele, T. G. & Staub, N. C. Alveolar shape changes with volume in isolated, air-filled lobes of cat lung. *J Appl Physiol* **28**, 411-414, doi:10.1152/jappl.1970.28.4.411 (1970).
23. Mertens, M. *et al.* Alveolar dynamics in acute lung injury: heterogeneous distension rather than cyclic opening and collapse. *Crit Care Med* **37**, 2604-2611, doi:10.1097/CCM.0b013e3181a5544d (2009).
24. D'Angelo, E. Local alveolar size and transpulmonary pressure in situ and in isolated lungs. *Respiration physiology* **14**, 251-266 (1972).
25. Flicker, E. & Lee, J. Equilibrium of force of subpleural alveoli: implications to lung mechanics. *Journal of applied physiology* **36**, 366-374 (1974).
26. Namati, E., Thiesse, J., de Ryk, J. & McLennan, G. Alveolar dynamics during respiration: are the pores of Kohn a pathway to recruitment? *American journal of respiratory cell and molecular biology* **38**, 572-578 (2008).
27. Greaves, I. A., Hildebrandt, J. & Hoppin Jr., F. G. in *Comprehensive Physiology* 217-231.

28. Gil, J., Bachofen, H., Gehr, P. & Weibel, E. Alveolar volume-surface area relation in air-and saline-filled lungs fixed by vascular perfusion. *Journal of Applied Physiology* **47**, 990-1001 (1979).
29. Sera, T. *et al.* Murine pulmonary acinar mechanics during quasi-static inflation using synchrotron refraction-enhanced computed tomography. *J Appl Physiol (1985)* **115**, 219-228, doi:10.1152/jappphysiol.01105.2012 (2013).
30. Matsuda, M., Fung, Y. & Sobin, S. Collagen and elastin fibers in human pulmonary alveolar mouths and ducts. *Journal of Applied Physiology* **63**, 1185-1194 (1987).
31. Mercer, R. R. & Crapo, J. Spatial distribution of collagen and elastin fibers in the lungs. *Journal of Applied Physiology* **69**, 756-765 (1990).
32. Oldmixon, E. & Hoppin Jr, F. Distribution of elastin and collagen in canine lung alveolar parenchyma. *Journal of Applied Physiology* **67**, 1941-1949 (1989).
33. Denny, E. & Schroter, R. C. Relationships between alveolar size and fibre distribution in a mammalian lung alveolar duct model. *J Biomech Eng* **119**, 289-297, doi:10.1115/1.2796093 (1997).
34. Suortti, P. *et al.* Fixed-exit monochromator for computed tomography with synchrotron radiation at energies 18-90 keV. *J Synchrotron Radiat* **7**, 340-347, doi:10.1107/s0909049500008384 (2000).
35. Bravin, A., Coan, P. & Suortti, P. X-ray phase-contrast imaging: from pre-clinical applications towards clinics. *Physics in medicine and biology* **58**, R1 (2013).
36. Percie du Sert, N. *et al.* The ARRIVE guidelines 2.0: Updated guidelines for reporting animal research. *Experimental Physiology* **105**, 1459-1466, doi:https://doi.org/10.1113/EP088870 (2020).
37. Fardin, L. *et al.* Imaging atelectrauma in Ventilator-Induced Lung Injury using 4D X-ray microscopy. *Sci Rep* **11**, 4236, doi:10.1038/s41598-020-77300-x (2021).
38. Mirone, A., Brun, E., Gouillart, E., Tafforeau, P. & Kieffer, J. The PyHST2 hybrid distributed code for high speed tomographic reconstruction with iterative reconstruction and a priori knowledge capabilities. *Nuclear Instruments and Methods in Physics Research Section B: Beam Interactions with Materials and Atoms* **324**, 41-48 (2014).
39. Paganin, D., Mayo, S. C., Gureyev, T. E., Miller, P. R. & Wilkins, S. W. Simultaneous phase and amplitude extraction from a single defocused image of a homogeneous object. *Journal of microscopy* **206**, 33-40 (2002).
40. Otsu, N. A threshold selection method from gray-level histograms. *IEEE transactions on systems, man, and cybernetic* **9**, 62-66 (1979).
41. Saitoh, T., Tamura, Y. & Kaneko, T. Automatic segmentation of liver region based on extracted blood vessels. *Systems and computers in Japan* **35**, 1-10 (2004).
42. Fan, L. & Chen, C. W. Reconstruction of airway tree based on topology and morphological operations. *Medical Imaging 2000: Physiology and Function from Multidimensional Images* **3978**, 46-57 (2000).
43. Klein, A. *et al.* in *Medical Imaging 2011: Image Processing*. 796220 (International Society for Optics and Photonics).

44. Heckemann, R. A. *et al.* Improving intersubject image registration using tissue-class information benefits robustness and accuracy of multi-atlas based anatomical segmentation. *NeuroImage* **51**, 221-227, doi:10.1016/j.neuroimage.2010.01.072 (2010).
45. Lee, T.-C., Kashyap, R. L. & Chu, C.-N. Building skeleton models via 3-D medial surface axis thinning algorithms. *CVGIP: Graphical Models and Image Processing* **56**, 462-478 (1994).
46. Zheng, Q. *et al.* in *Computer Graphics Forum*. 635-644 (Wiley Online Library).
47. Leow, A. D. *et al.* Statistical properties of Jacobian maps and the realization of unbiased large-deformation nonlinear image registration. *IEEE transactions on medical imaging* **26**, 822-832 (2007).
48. Dilts, G. A. Moving-least-squares-particle hydrodynamics-I. Consistency and stability. *International Journal for Numerical Methods in Engineering* **44**, 1115-1155 (1999).
49. Wernersson, E. L., Hendriks, C. L. L. & Brun, A. in *2011 International Conference on 3D Imaging, Modeling, Processing, Visualization and Transmission*. 312-317.

## Figures

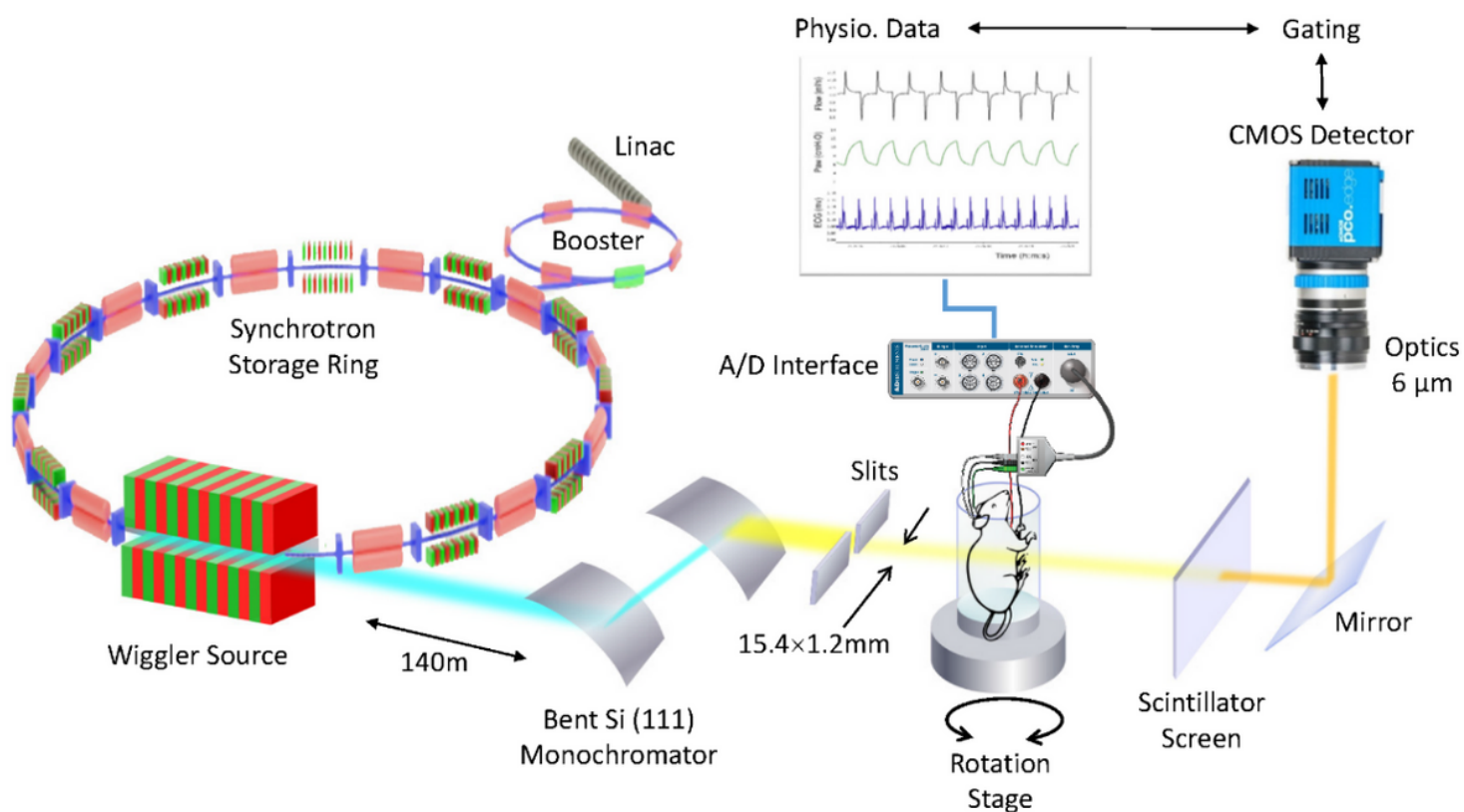


**Figure 1**

Dynamic 3D microscopy of rat lung using a synchrotron X-ray source. High-intensity coherent X-rays generated from electrons orbiting in a storage ring, are rendered monochromatic using bent silicon crystal optics, and detected by a PCO Edge 5.5 camera coupled to a Cerium-doped Lutetium Aluminium Garnet

(LuAG:Ce) scintillator and optics yielding an isotropic pixel size of  $6 \mu\text{m}^3$ . The in vivo anesthetized rat is mechanically ventilated while the electrocardiogram and respiration are monitored and recorded.

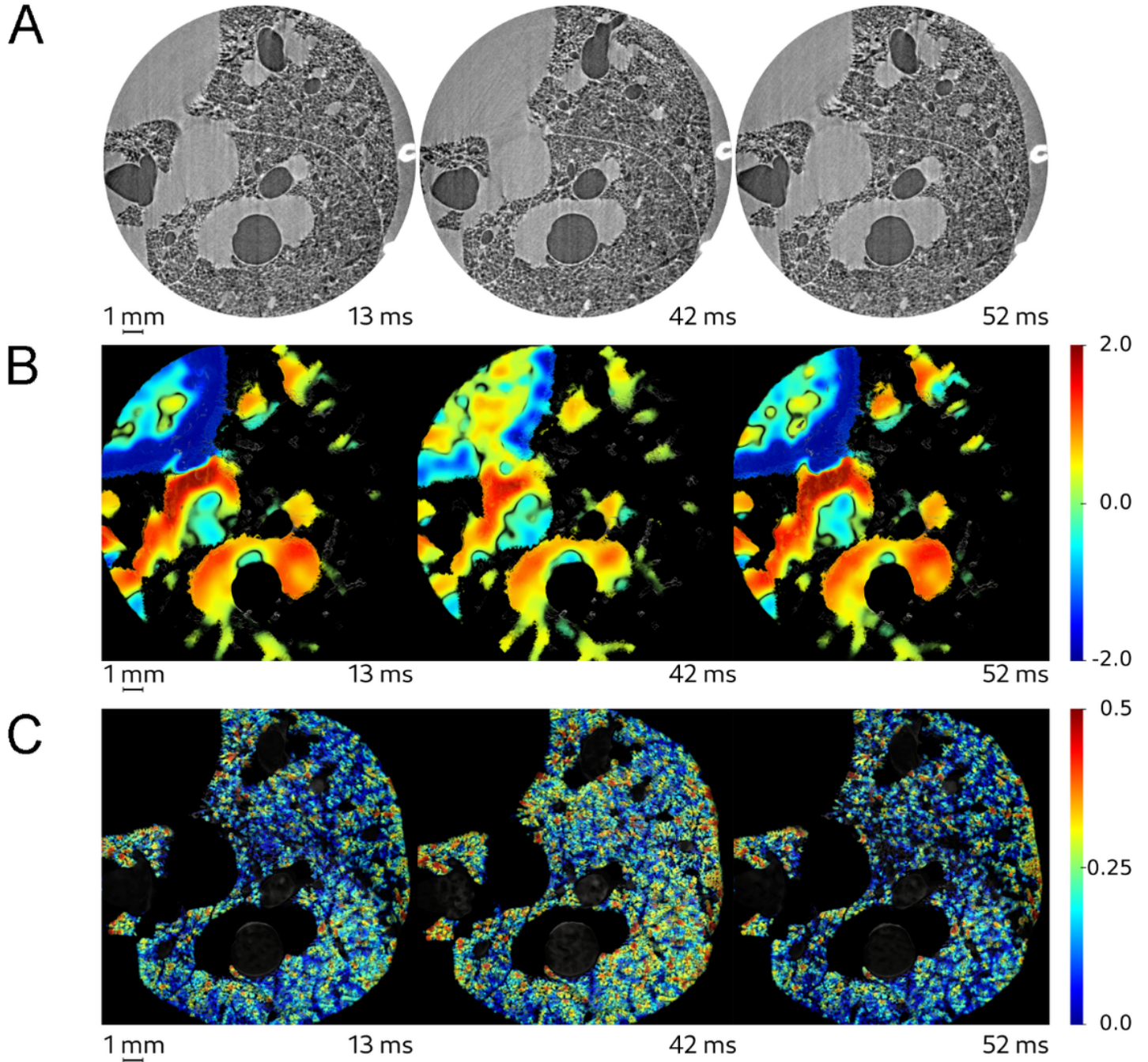


**Figure 2**

Dynamic 3D microscopy of rat lung using a synchrotron X-ray source. High-intensity coherent X-rays generated from electrons orbiting in a storage ring, are rendered monochromatic using silicon crystal optics, and detected by a PCO Edge 5.5 camera coupled to a Cerium-doped Lutetium Aluminium Garnet scintillator and optics giving an isotropic pixel size of  $6 \mu\text{m}^3$ . The in vivo anesthetized rat is mechanically ventilated while the electrocardiogram is monitored.

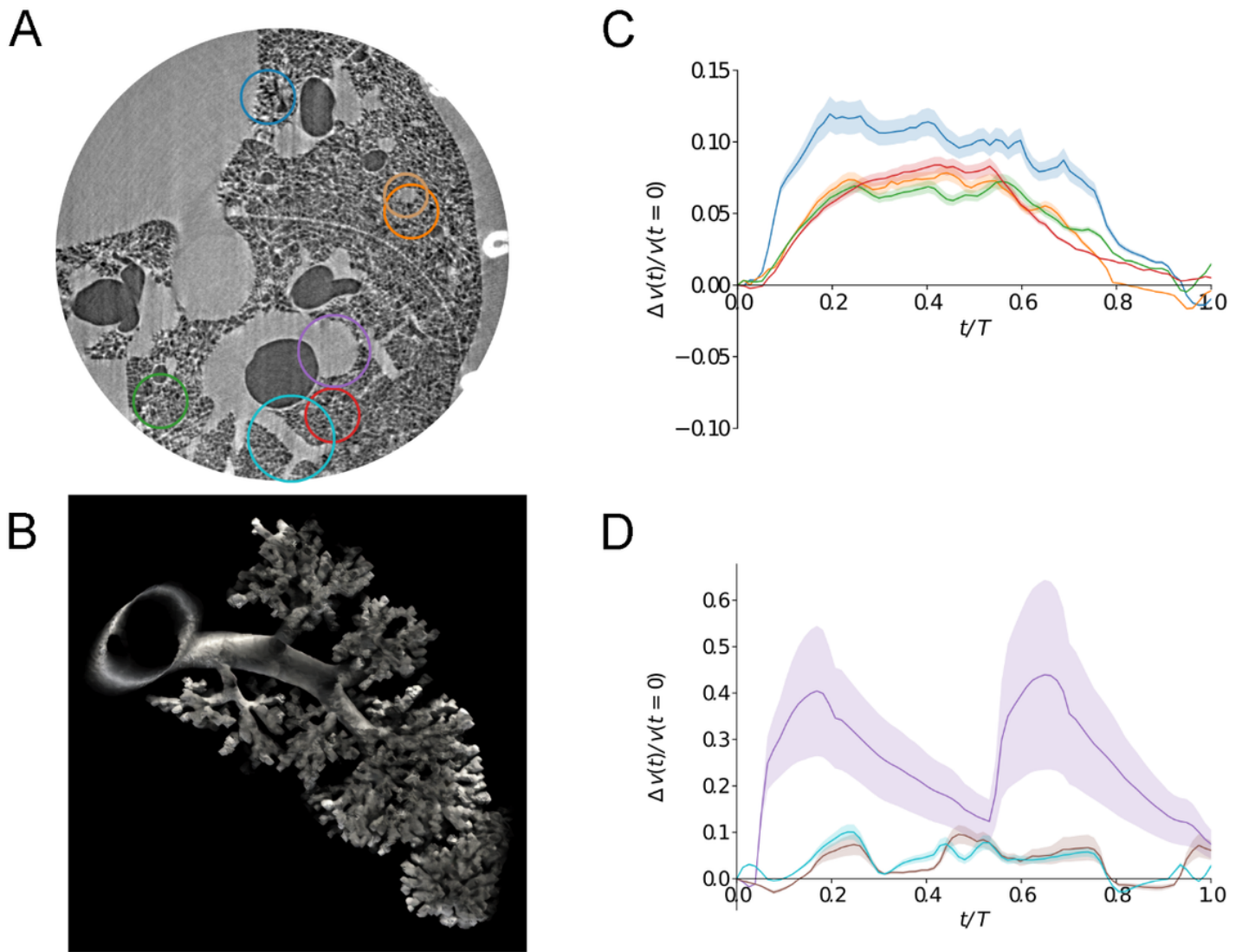


**Figure 3**

A: X-ray CT image of live rat lung. Colored circles show regions of interest where regional biomechanics are computed; B: a segmented airway with subtending conducting airways and terminal acinar structures at end-expiration in a live rat; C: regional strain as a function of time computed within airspaces in the regions of interest of same color as in A. The shaded area represents within-ROI standard deviation; D: regional strain as a function of time computed within blood vessels in the regions of interest shown in A. The shaded area represents within-ROI standard deviation. Note the typical pulse-wave deformation within the larger artery which is significantly damped in smaller caliber vessels.

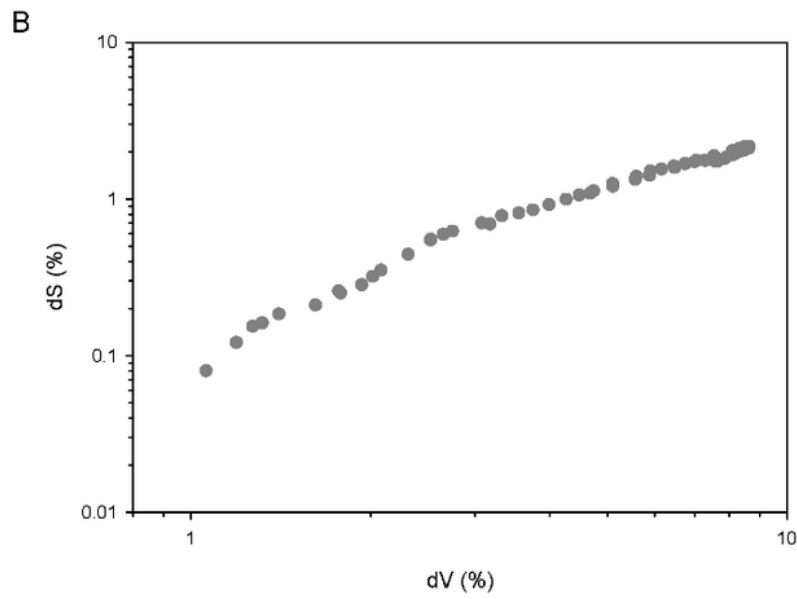
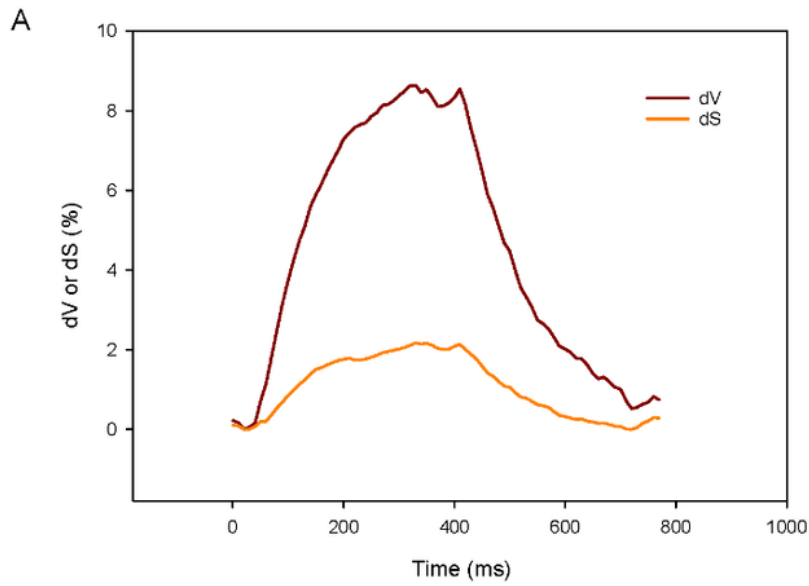


**Figure 4**

A: Relative surface and volume change of peripheral airspaces within a sample ROI; B: Log-Log relation between changes in surface (S) and volume (V).

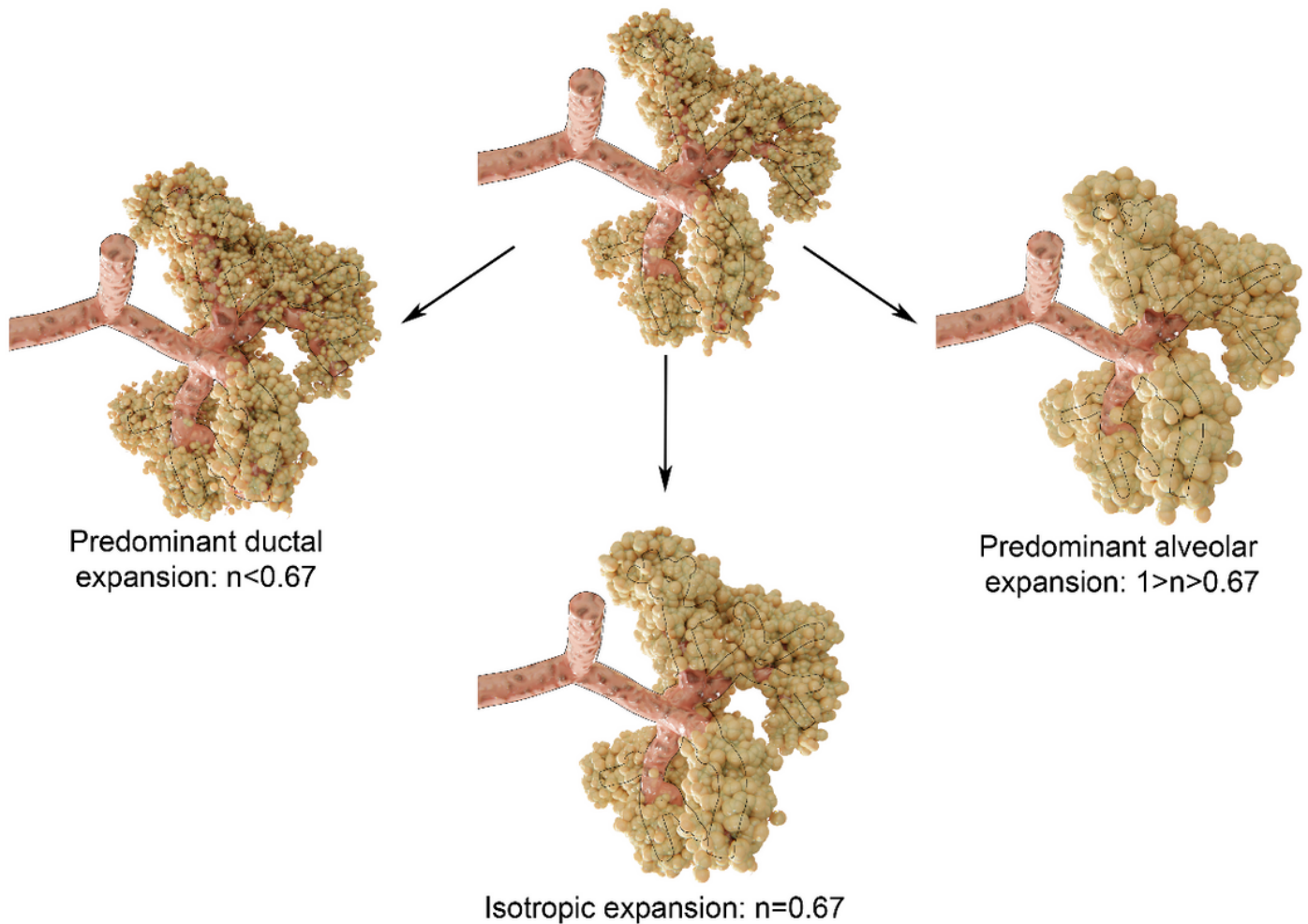


**Figure 5**

Schematic representation of how different acinar conformational changes translate into the exponent  $n$  in  $S = kV^n$ . Thin black lines delineate approximate alveolar ductal size. Isotropic balloon like expansion results in  $S = kV^{2/3}$ , while a predominantly ductal expansion (50% increase in radius) would cause  $n$  to be  $< 2/3$  or  $< 0.67$ , and a predominantly alveolar expansion (50% increase in radius) would increase  $n > 0.67$ .

## Supplementary Files

This is a list of supplementary files associated with this preprint. Click to download.

- [SupportingInformation.docx](#)
- [divanim.mp4](#)
- [divanimvessels2.mp4](#)
- [greyanim.mp4](#)